A quantum mechanical model of field emission from a graphene blade type material.

Bruno Lepetit

A quantum mechanical model of field emission from a graphene blade type material.

Bruno Lepetit*

Laboratoire Collisions Agrégats Réactivité, UMR5589,

Université Toulouse III Paul Sabatier, CNRS,

Bât. 3R1b4 - 118 route de Narbonne 31062 Toulouse Cedex 09, France

(Dated: March 10, 2023)

Abstract

We present a simple quantum perturbative full dimensionality model to study field emission from a graphene blade within the frame of the Bardeen transfer Hamiltonian formalism. The material electronic wavefunction is obtained for a multidimensional square well potential specifically designed to reproduce 2 important characteristics of the material, the Fermi level and the shape of the emitting orbitals. The wavefunction in the vacuum between the electrodes is obtained with a close coupling method in a finite domain. Our model provides the emitted current density with respect to the applied field. This allows to discriminate the different functional forms proposed to fit the Fowler-Nordheim emission curves. Our model also provides information on emission patterns. Electron total energy distributions are computed for different field intensities and compared with other theoretical and experimental results.

I. INTRODUCTION

Graphene field emission has been the subject of numerous experimental and theoretical studies (reviewed in ref. 1–4) which shed some light on the physical processes which give rise to electron emission but at the same time leave many questions unanswered. On the experimental side, there is a dearth of measurements on well characterized graphene samples, indeed it is often not fully clear how clean the sample is at the end of the conditioning process. As a result, different studies sometimes produce somewhat contradictory results. For instance, in ref. 5, emission was shown to be small near the center of graphene flakes but large near its edges, as expected. However, in other experiments, significant current levels were extracted from the central flat part of individual single- and few-layer graphene flakes[6,7]. Interesting electron emission patterns (lip patterns) were observed as pairs of ovals separated by central dark lines[8,9] but these patterns were shown to depend strongly on the emitting surface cleanliness[10]. Emitted electron energy spectra (often called total energy distributions : TED) were recorded but the energy distribution widths differ by something like an order of magnitude between different studies[10,11].

No unifying picture emerges either from the different theoretical studies performed on this problem. The original Fowler-Nordheim model (FN)[12] and its subsequent refinements[13–19] still form nowadays the dominant paradigm to understand electronic field emission even for reduced dimensionality materials like graphene. These models provide in particular a linear relation between $\log(I/F^2)$ and $1/F$, where I is the emitted current and F the applied electric field. They have been challenged more recently by 2 dimensional (2D) models specific to planar materials which provide alternative relations between emitted current and field[2,20–22]. Moreover, modifications of the FN model to describe emission from the edges instead of the flat part of 2D materials also provide new relations between current and field[23]. Whereas all these models rely on a crude description of the material electrons, more elaborate ones using time dependent (TDDFT) or stationary (DFT) density functional theory were also implemented in the context of graphene emission. TDDFT calculations showed that dangling bonds are major contributors to field emission currents and that H terminations reduce them[24–26]. Other DFT studies showed that adsorption of functional chemical groups could have strong effects on emission[27–29]. Occasionally, some of these calculations provided intriguing results, for instance the possibility of large emission for energies far below the

Fermi level[24,25]. Interestingly, whereas TDDFT calculations[24,25] provide broad TEDs (width $\Delta E \approx 1$ eV), DFT ones[26] provide one order of magnitude narrower TEDs. Concerning emission patterns, "dragon-fly"-type ones were computed[30,31], in contrast with the observed "lip" ones[8,9].

The present studies aims at clarifying several issues related to graphene blade emission. We will first revisit the emission pattern issue and provide a simple intuitive picture for it. Then, we will consider how well the Fowler-Nordheim law applies to emission from edges : should we use the standard law or an improved one as proposed in ref. 23 ? A final issue will be the TED width : can we provide some consistency to the different results available ? To achieve these goals, we propose a simple graphene blade model where the focus is not accuracy, but simplicity from which clarification is expected to emerge. We extend to the present blade configuration the perturbative method developed recently to describe emission from metals[32–34] and then from a graphene plane[21]. It relies, first on a separate description of external (vacuum) and internal (material) regions, second on a perturbative coupling between both. This method is described in section II, the computational results in section III, focusing on the three main issues - emission patterns, FN laws, TED widths - mentioned above.

II. METHOD

A. Material region

We consider a graphene blade section A of area $L_x\,L_z$ located in the $(x \leq 0, z)$ half-plane and perpendicular to the y axis. The edge corresponds to $x = y = 0$. In the absence of external electric field, electrons are confined in a thin shell around A of thickness L_y by the intrinsic material electrostatic potential which we assume to be independent of z : $V_i(x,y,z) = V_0$ ($V_0 > 0$) when $-L_x \leq x \leq 0$ and $-\frac{L_y}{2} \leq y \leq \frac{L_y}{2}$, $V_i(x,y,z) = 0$ otherwise. Approximate analytical electronic wavefunctions associated to the confining potential $-qV_i(x,y,z)$ ($q > 0$ is the absolute value of the electron charge) are obtained by assuming separability, as shown in appendix A. The material electronic wavefunction then reads :

$$\Phi_{n_x\,n_y\,n_z}(x,y,z) = \phi_{n_x\,n_y}(x,y)\,\varphi_{n_z}(z) \tag{1}$$

with: $\varphi_{n_z}(z) = \frac{1}{L_z^{\frac{1}{2}}} e^{ik_{n_z}z}$ and: $k_{n_z} = n_z \frac{2\pi}{L_z}$, n_z integer. The integers n_x and n_y are the quantum numbers associated to the discrete levels bound in the one dimensional potentials along x and y. In the present study, we use exclusively the first antisymmetric y state (nodal plane $y = 0$) to mimic the carbon π orbitals perpendicular to the xz graphene plane. Thus we have always $n_y = 1$ and we drop this quantum number in the following equations to simplify notations.

The 2 parameters which define the well along y, V_0 and L_y, are chosen in order to model graphene reasonably well by imposing two conditions. First, we compute the average y distance associated to the wavefunction of eq. 1 and we adjust the potential to obtain an average $\bar{y}$ value close to the reference value given by ref. 35 : $\bar{y}$=0.074 nm. Second, we impose that the Fermi level energy should be close to the experimental value[21] $\epsilon_F = -W$=-4.5 eV, where W is the work function. The Fermi level energy can be obtained implicitly from the relation :

$$\sigma_e = \frac{2}{\pi L_x} \sum_{n_x/\epsilon_{n_x} \leq \epsilon_F} \left(\frac{2m(\epsilon_F - \epsilon_{n_x})}{\hbar^2} \right)^{\frac{1}{2}} \tag{2}$$

where σ_e is the electronic density, ϵ_{n_x} the energy associated to $\phi_{n_x}(x, y)$, m the electron mass and $\hbar$ the Planck constant. This equation expresses the fact that to each discrete level ϵ_{n_x} corresponds a one dimensional continuum of planes waves along z which are doubly occupied up to the Fermi level. In the case of graphene, there are two π_y electrons per unit cell - one for each of the 2 atoms of the cell - the area of which is $A_{uc} = \frac{3\sqrt{3}}{2}a^2$ where a is the hexagonal cell parameter : $a = 0.142$ nm. The electron density is : $\sigma_e = \frac{2}{A_{uc}}$=38.18 e^-/nm^2. Knowing the electron density and the energy spectrum, the Fermi energy is obtained. The parameters defining the potential well, its depth V_0 and its width L_y, have a direct impact on the orbital shapes and thus on $\bar{y}(V_0, L_y)$, as well as on the energy spectrum and thus on $\epsilon_F(V_0, L_y)$. The constraint that $\bar{y}(V_0, L_y)$ has a specific value is satisfied on a line in the (V_0, L_y) parameter plane, and similarly, the desired value of $\epsilon_F(V_0, L_y)$ is obtained on another line in the same plane. The intersection of both lines is the point where both constraints are satisfied. In practice, this point has been found after many numerical evaluations of $\bar{y}(V_0, L_y)$ and $\epsilon_F(V_0, L_y)$ in the parameter plane. With the choice : $V_0 = 35.70$ eV and $L_y = 0.186$ nm, we obtain : $\bar{y}$=0.073 nm and : $\epsilon_F = -4.50$ eV. Both values are very close to the target. Notice that the Fermi energy ϵ_F has a weak dependence on L_x and that the present value has been obtained for $L_x = 100$ nm.

Our approach is close to the one presented in ref. 36, but differs in the second constrain which they choose as : $\epsilon_0 = -W$, i.e. the band bottom is at the Fermi level energy. In fact we have : $\epsilon_0 = -(W + W_B)$ where the band width is[21] : W_B=8.4 eV. Besides, notice that we made no attempt to reproduce the graphene dispersion relation which leads to a Dirac cone in the vicinity of the K point in reciprocical space[37]. Indeed, we showed in a previous study[21] that the details of the emission band are unimportant for field emission.

B. Inter-electrode region

The half-plane cathode is now facing an anode which is represented by a parabolic cylinder of axis z defined by the equation : $r + x = 2x_a$, $r = (x^2 + y^2)^{\frac{1}{2}}$ for a given positive x_a which is the distance between the parabola vertex (located on the x axis) and the blade edge. The electrode system geometry is shown on fig. 1. This approximate planar anode provides a simple analytical inter-electrode electrostatic potential in terms of the parabolic cylinder coordinates $(\lambda > 0, \mu, z)$:

$$x = \frac{1}{2}\left(\lambda^2 - \mu^2\right) \qquad y = \lambda\mu \tag{3}$$

The anode equation is then $\lambda = \lambda_a = (2x_a)^{\frac{1}{2}}$ and the cathode one : $\lambda = \lambda_c = 0$. We assume for this part of the problem a zero thickness cathode (L_y=0) which is justified by the fact that L_y is much smaller than the other dimensions of the problem, namely the cathode-anode distance and the anode width. However, as L_y is of the same order of magnitude as a typical tunneling length, setting L_y=0 may have some impact of the inter-electrode wavefunction, especially in the close vicinity to the cathode. We assume that the problem is confined transversely by the condition $\mu \leq \mu_M$.

The inter-electrode electrostatic potential $V_e(\lambda, \mu, z)$ is solution of the Laplace equation with boundary conditions : $V_e(\lambda = 0, \mu, z) = 0$ at the cathode and $V_e(\lambda = \lambda_a, \mu, z) = V_{ea}$ at the anode ($V_{ea} > 0$) and is a function of λ only given by :

$$V_e(\lambda) = V_{ea}\frac{\lambda}{\lambda_a} \tag{4}$$

The corresponding electric field is :

$$\vec{\mathbf{F}}(\lambda, \mu) = -\frac{V_{ea}}{\lambda_a(\lambda^2 + \mu^2)^{\frac{1}{2}}}\vec{\boldsymbol{\lambda}} = -F_a\left(\frac{x_a}{r}\right)^{\frac{1}{2}}\vec{\boldsymbol{\lambda}} \tag{5}$$

where F_a is the amplitude of the field at the anode vertex and where $\vec{\boldsymbol{\lambda}}$ is defined from the usual Cartesian $(\vec{\mathbf{x}}, \vec{\mathbf{y}})$ frame by : $\vec{\boldsymbol{\lambda}} = \frac{1}{(\lambda^2+\mu^2)^{\frac{1}{2}}}(\lambda\vec{\mathbf{x}} + \mu\vec{\mathbf{y}})$. The emitting properties of the material are expected to depend mainly on the local field in its vicinity and not from the far field. As a result, although a parabolic anode was selected here for simplicity, we expect our conclusions to be transposable without major changes to other systems including anodes with different shapes.

The motion of an electron emitted from the cathode in the inter-electrode region is driven by the Hamiltonian :

$$H = -\frac{\hbar^2}{2m(\lambda^2+\mu^2)}\left(\frac{\partial^2}{\partial\lambda^2} + \frac{\partial^2}{\partial\mu^2}\right) - \frac{\hbar^2}{2m}\frac{\partial^2}{\partial z^2} - qV_e(\lambda). \tag{6}$$

If this electron is emitted from an initial material state $\Phi_{n_x\, n_z}$ (eq. 1), it is described in the inter-electrode region by an eigenstate of this Hamiltonian: $\Psi_{\epsilon_{n_x n_z}}(\lambda, \mu, z; V_{ea}) = \psi_{\epsilon_{n_x}}(\lambda, \mu; V_{ea})\varphi_{n_z}(z)$, with the same energy $\epsilon_{n_x n_z}$ as in the material and the same momentum along z if we neglect all dissipative processes like electron-electron or electron-phonon interactions during emission. This wavefunction depends parametrically on V_{ea}. We describe in appendix B the technicalities implemented in this work to obtain the 2 dimensional wavefunction $\psi_{\epsilon_{n_x}}(\lambda, \mu; V_{ea})$, inspired by methods routinely used in the field of quantum scattering theory (ref. 38 and references therein). This wavefunction is obtained by expansion on a basis of N channel states (defined in the appendix), N being chosen large enough for convergence to be achieved. In the space spanned by this basis, there are in fact not a single, but a set of N wavefunctions $\Psi_{\epsilon_{n_x n_z}}(\lambda, \mu, z; V_{ea})$ which are eigenfunctions of the inter-electrode Hamiltonian, each corresponding to different boundary conditions associated to the scattering (S)-matrix. To emphasize the role of the boundary conditions, these 3 dimensional wavefunctions are labeled $\Psi^{(S)}_{n_0\,\epsilon_{n_x n_z}}(\lambda, \mu, z; V_{ea})$ in the following and the corresponding 2 dimensional ones $\psi^{(S)}_{n_0\,\epsilon_{n_x}}(\lambda, \mu; V_{ea})$ with $n_0 = 1 - N$.

C. The Bardeen formalism

In a quantum mechanical perturbative framework, electron emission results from the coupling between the unperturbed material $\Phi_{n_x\, n_z}$ and vacuum $\Psi_{n_0\,\epsilon_{n_x n_z}}$ wavefunctions described in the 2 preceding paragraphs. As we neglect all energy exchange between electrons and the lattice, emitted electron initial and final states have the same energy $\epsilon_{n_x n_z}$ smaller

than the Fermi energy of the material : $\epsilon_{n_x n_z} \leq \epsilon_F$. Following Bardeen's prescription[39], the emitted current is obtained by integration over a properly chosen dividing surface $\lambda = \lambda_0$ (eq. 1 in ref. 21):

$$I(V_{ea}) = 2 \sum_{n_x\, n_z/\epsilon_{n_x n_z} \leq \epsilon_F, n_0=1,N} I_{n_0 n_x n_z}(V_{ea}) \tag{7}$$

where the x 2 prefactor in the definition of $I(V_{ea})$ accounts for spin degeneracy with

$$I_{n_0 n_x n_z}(V_{ea}) = q\frac{2\pi}{\hbar}\left| \int\int_{(\mu,z)\in A} d\mu dz M_{n_0 n_x n_z}(\lambda_0, \mu, z; V_{ea}) \right|^2 \tag{8}$$

$M_{n_0 n_x n_z}$ is given by :

$$M_{n_0 n_x n_z}(\lambda_0, \mu, z; V_{ea}) = \tag{9}$$
$$\frac{\hbar^2}{2m}\left(\Psi^{(S)}_{n_0\, \epsilon_{n_x n_z}}(\lambda_0, \mu, z; V_{ea})^* \frac{\partial \Phi_{n_x n_z}(\lambda_0, \mu, z)}{\partial \lambda} - \Phi_{n_x n_z}(\lambda_0, \mu, z) \frac{\partial \Psi^{(S)}_{n_0\, \epsilon_{n_x n_z}}(\lambda_0, \mu, z; V_{ea})^*}{\partial \lambda} \right)$$

where * refers to complex conjugation. As $\Phi_{n_x n_z}$ is known analytically in cartesian coordinates (eq. 1), finding its values in terms of parabolic coordinates is straightforward. As $M_{n_0 n_x n_z}$ is in fact independent of z and n_z, eqs. 8 can be simplified into:

$$I_{n_0 n_x n_z}(V_{ea}) = I_{n_0 n_x}(V_{ea}) = q\frac{2\pi}{\hbar}\left| \int_{\mu\in A} d\mu\, m_{n_0 n_x}(\lambda_0, \mu; V_{ea}) \right|^2 \tag{10}$$

with :

$$m_{n_0 n_x}(\lambda_0, \mu; V_{ea}) = \frac{\hbar^2}{2m}\left(\psi^{(S)}_{n_0\, \epsilon_{n_x}}(\lambda_0, \mu; V_{ea})^* \frac{\partial \phi_{n_x}(\lambda_0, \mu)}{\partial \lambda} - \phi_{n_x}(\lambda_0, \mu) \frac{\partial \psi^{(S)}_{n_0\, \epsilon_{n_x}}(\lambda_0, \mu; V_{ea})^*}{\partial \lambda} \right) \tag{11}$$

Summing over n_z in eq. 7 we obtain finally:

$$I(V_{ea}) = 2L_z \frac{(2m)^{\frac{1}{2}}}{\pi\hbar} \sum_{n_x/\epsilon_{n_x} \leq \epsilon_F, n_0=1,N} (\epsilon_F - \epsilon_{n_x})^{\frac{1}{2}}\, I_{n_0 n_x}(V_{ea}) \tag{12}$$

λ_0 is chosen to maximize $I_{n_0 n_x}$. Near its maximum, $I_{n_0 n_x}$ has the weakest possible dependence on λ_0, this is why this dependence has been dropped in the equations above.

D. Convergence

The anode is assumed to be at a distance x_a=100 nm from the cathode and its potential V_{ea} is adjusted using eq. 5 to achieve a target field F_a at its vertex (y=0). As we increase

the blade length L_x, we find that the current density becomes independent of this parameter for L_x larger than $L_x \approx$ 20-30 nm, which corresponds to typical blade sizes used to obtain the results shown below. The wavefunction given by eq. B8 is computed numerically in the finite domain $|\mu| \leq \mu_M$ and $0 \leq \lambda \leq \lambda_M$ which is bounded in the x, y plane by 2 parabolas. One is turned toward negative x and its vertex is located at $x_{max} = \lambda_M^2/2$, $y = 0$. The second parabola is turned toward positive x and its vertex is at : $x_{min} = -\mu_M^2/2$,$y = 0$. When $\mu \geq \mu_M$, we have $\psi^{(S)}_{n_0\,\epsilon_{n_x}}(\lambda, \mu; V_{ea}) = 0$ and when $\lambda \geq \lambda_M$, $\psi^{(S)}_{n_0\,\epsilon_{n_x}}(\lambda, \mu; V_{ea})$ is obtained from the asymptotic forms given by eq. B7-B9. λ_M and μ_M are increased until convergence is reached, this was achieved for x_{min}=-3 nm, x_{max}= 5 nm. Inside the domain, N =12 wavefunctions obtained by expansion on a set containing the same number N of channel functions $s_n^{\epsilon_{n_x}}(\mu; \lambda)$ (eq. B8) were found to be sufficient for convergence. These channel functions are obtained in turn by expansion on a set of 60 primitive states $s_n^0(\mu)$ (eq. B2) generated on a grid of 60 μ-points.

Fig. 2 provides some hints why convergence is achieved in the domain bounded by λ_M and μ_M, although its size is small with respect to L_x and the inter-electrode distance x_a. The graphene blade wavefunction squared $|\Phi_{n_x n_z}|^2$ is localized mainly in the graphene blade domain $x \leq 0$, $y \leq L_y/2 = 0.093$ nm (section II A) but also extends further in the classically forbidden region. It nodal system along x is associated to a standing wave oscillating between both sides of the blade separated by the distance L_x. It has a shape along y characteristic of π_y orbitals by design, with opposite sign lobes for $y > 0$ and $y < 0$ (not shown). On the other hand, the inter-electrode wavefunction $|\psi^{(S)}_{n_0\,\epsilon_{n_x}}(\lambda, \mu; V_{ea})|^2$ extends mainly in the classically allowed region with respect to the inter electrode electrostatic potential (at the right of the black dashed line). As a result, the Bardeen overlap squared $|m_{n_0 n_x}(\lambda, \mu; V_{ea})|^2$ between both functions is highly localized in a band of length less 1 nm along x and nearly 0.1 nm along y. This indicates that emission is significant only in the close vicinity of the edge and that it is sufficient to know the inter-electrode wavefunction in a volume much smaller than the blade width L_x and than the inter-electrode distance x_a.

The dividing surface parametrized by $\lambda = \lambda_0$ (section II C) is also a parabola turned toward negative x with a vertex $x_0 = \lambda_0^2/2 = 0.042$ nm, y=0 for $F_a = 0.5$ V/nm. It is very close to the material because its wavefunction $\Phi_{n_x n_z}$ vanishes quickly away from the material. Finally, the number of n_x terms involved in the sum of eq. 12 increases with L_x and is 55 for $L_x = 30$ nm : this is the number of states ϕ_{n_x} with energy ϵ_{n_x} larger than

-10 eV below vacuum (material states with energy lower than this threshold contribute negligibly to emission) and smaller than the Fermi energy (we assume that the material temperature is 0 K).

III. RESULTS

A. Emission patterns

The squared Bardeen overlap $|m_{n_0 n_x}(\lambda, \mu; V_{ea})|^2$ shown on fig. 2 gives the location of the bright spots from which electron emission is significant. The 2 main emitting spots closest to the blade edge are located at $y \approx 0.1$ nm and the other one by symetry at $y \approx$ -0.1 nm (not shown on the figure). These locations correspond to maximum overlaps between the evanescent material wavefunction and the vacuum one. Notice that the material wavefunction penetrates deeper in the classically forbidden region along y than along x. This is a consequence of the partition of the kinetic energy along x and y : it is smaller along x (= 9.15 eV) than along y (= 22.05 eV), although the excitation quantum number is higher along x (for the figure : $n_x = 98$) as compared to y ($n_y = 1$). Interestingly, the brightest emission spots are not located on the blade plane ($y = 0$) which, on the contrary, corresponds to a nodal plane. This is related to the symmetry of the graphene π orbitals, which point along y perpendicularly to the graphene plane and have 2 lobes of opposite signs on both sides of the material plane.

These spots emit electron beams in vacuum which eventually are collected on a screen and produce images which were recorded in several experiments[8–10,40]. Their patterns depend on the properties of the emitting spots and of the electric field experienced by the electrons between cathode and screen. They consist typically in several more or less aligned pairs of ovals, the ovals of each pair being separated by a central dark line which gives the image a "lip pattern" also called "strip pattern". The central dark line is interpreted as the result of destructive interferences between the electron beams emitted from both sides of the edge which have opposite phases because they correspond to the opposite lobes of the carbon π orbitals. This interpretation is supported by the model of ref. 30 as well as the present one. A picture of the observed patterns and their orientation with respect to the cathode is shown on fig. 3.

Two interpretations are given in the literature for the alignment of the oval pairs. According to ref. 40, this array may result from interferences between electron beams emitted coherently by several emission sites along the edge. These interferences are different from those which occur within each beam and which produce the dark zone in the middle of each elongated form. On the other hand, according to ref. 9, it corresponds to separate images of different emission sites aligned on the edge, separated by approximately 0.14-0.22 nm, which is typical of distances between carbon atoms along the edge. The interference hypothesis assumes that the different beams diverge and overlap significantly, whereas the separate image hypothesis assumes non-overlapping narrow beams. Our model provides information on the beam divergence shown on fig. 4 as a distribution of θ_z, the angle between the z-axis and xy-plane components of the emitted electron speeds. This distribution is obtained in a classical picture from the knowledge of the kinetic energy of the emitted electrons along the z direction (ϵ_z^k) and in the xy plane (ϵ_{xy}^k) : $\tan(\theta_z) = \left(\frac{\epsilon_z^k}{\epsilon_{xy}^k}\right)^{\frac{1}{2}}$. The distributions, maximum for θ_z=0, are narrow but broaden as field increases. In fact, the tunneling potential barrier which the electrons experience while being extracted from the edge acts as a low v_z filter. Indeed, for a given total energy, electrons with less kinetic energy along z have more kinetic energy available along x, which favors tunneling. Divergence of the beam is expected to be smaller when it is collected on the screen. Indeed, as the electric field has no component perpendicular to the xy in our model, ϵ_{xy}^k increases in the travel from the edge to the screen, whereas ϵ_z^k remains unchanged. We conclude that the electron beam collected on the screen is narrow in the direction parallel to the edge, but a more realistic study would be required to state whether it is sufficiently narrow to provide an image resulting from separate beams, or if the image results from the interference of overlapping beams.

Notice finally that the step-like character of the distribution on fig. 4 is due to the finite blade size L_x. Indeed, each discrete level with energy ϵ_{n_x} can be occupied by electrons having along z a maximum kinetic energy $\epsilon_F - \epsilon_{n_x}$ and this maximum obviously decreases as ϵ_{n_x} increases. As a result, the maximum θ_z for the electrons associated to ϵ_{n_x} decreases also as ϵ_{n_x} increases and each step corresponds to one of these maxima. Considering larger blades would produce smoother distributions.

B. Fowler Nordheim plots

Fig. 5 provides a usual FN plot of $ln(j(F_a))/F_a^2$ as a function of $1/F_a$, where $j(F_a)$ is the current density obtained from eq. 12 : $j(F_a) = \frac{I(V_{ea})}{L_z}$; it is of course independent of L_z. A local field enhancement factor β_W could be obtained from a linear fit of this curve using the usual expression for the slope :

$$s = -\frac{4}{3}\left(\frac{2m}{\hbar^2}\right)^{\frac{1}{2}} \frac{W^{\frac{3}{2}}}{q\beta_W}. \tag{13}$$

However, fig. 5 shows that plotting $ln(j(F_a))$ instead of $ln(j(F_a))/F_a^2$ as a function of $1/F_a$ provides a better quality linear fit. The coefficient of determination r^2 (eq. 15.2.13 and 14.5.1 in ref. 41) is indeed r^2= 0.999 for $ln(j(F_a))$ and it is slightly less (r^2= 0.992) for $ln(j(F_a))/F_a^2$. Using eq. 13 for the slope of the linear fit of $ln(j(F_a))$, we obtain $\beta_W = 13.$ if we use W=4.5 eV for the work function. In fact, we did not expect to obtain a good fit with the usual Fowler-Nordheim functional form as we are very far from the flat emission surface hypothesis with the present low radius of curvature emitter.

The present electrostatic model gives another enhancement factor which from eq. 5 is : $\beta_E = \left(\frac{x_a}{r}\right)^{\frac{1}{2}}$. It diverges at the blade tip r=0. The distances r_W for which $\beta_E = \beta_W$ for x_a=100 nm is r_W=0.59 nm. The best electrostatic enhancement factor is expected to correspond to the location where emission is maximum. From fig. 2, this occurs for $x \approx 0$, $y \approx 0.1$ nm which corresponds to β_E=32, which is of the same order of magnitude as β_W.

The present enhancement factors, β_W and β_E, can be compared with other electrostatic calculation results. Ref. 42 proposes analytical formulas fitting electrostatic numerical simulation results, they obtain $\beta \approx 1.77\left(\frac{L_x}{L_y}\right)^{0.75}$ which gives β=80. (L_x =30 nm, L_y =0.186 nm). In ref. 23, an analytical solution based on a conformal transformation is proposed and in the limit of a thin blade it provides (eq. 5.14) : $\beta \approx \left(\frac{\pi}{2}\frac{L_x}{L_y}\right)^{\frac{1}{2}}$=16. All these results are of the same order of magnitude, although the geometry of our problem is somewhat different from the one of ref. 23,42, where the blade is placed perpendicularly on an infinite plane.

Ref. 23 also proposes adaptations of the general FN law to the nanowall case. It is suggested to substitute to the work function W the effective barrier height H : $H = W + \frac{\hbar^2 k_{n_y=1}^2}{2m} = 26.55$ eV. This accounts for the fact that the kinetic energy trapped in the y motion (= 22.05 eV, see section III A) is supposedly not able to promote emission which would take place exclusively along the x direction. Ref. 23 provides analytical expressions for emitted

currents in 2 limiting cases, the "slowly varying field limit" when the thickness L_y of the blade is large with respect the tunneling barrier length l, and the "sharply varying field limit" in the opposite situation. In the present case, if we define the tunneling barrier length as the minimum distance between turning point lines (the distance along x between both dashed lines on fig. 2) then $l \approx 0.2$ nm so that $l \approx L_y$ and so that the present case represents an intermediate situation between both limits. In the "slowly varying field limit", a linear relation between $ln(j)/F_a^{\frac{3}{2}}$ and $1/F_a$ is expected (eq. 6.14 in ref. 23). The linear fit of these data (not shown) provides r^2= 0.995, which is slightly better than the fit for $ln(j)/F_a^2$, but worse than for $ln(j)$ (fig. 5). The slope is still given by eq. 13 with H instead of W and the resulting enhancement factor β_H is : $\beta_H = 223$. This is presumably an overestimate of the true enhancement. Indeed, as fig. 2 shows, emission takes place mainly from the corner $y \approx 0.2$ nm and not from the plane $y \approx 0$ plane which would correspond to electrons emitted with velocity along x exclusively. As a result, the kinetic energy associated to the y motion can also contribute to emission. Indeed, if we use eq. 13 with the original W instead of H to model the "slowly varying field limit" slope, we obtain : $\beta = 16.$, in better agreement with the previous results.

In the "sharply varying field limit", a linear relation between $ln(j/F_a^3)$ and $1/F_a^2$ is expected and the corresponding slope is (eq. 6.15 in ref. 23) : $s = -\frac{2^{\frac{7}{2}}}{15}\frac{m^{\frac{1}{2}}}{q^2\hbar L_x}H^{\frac{5}{2}}$. The linear fit of the corresponding curve (fig. 6) has a coefficient of determination very close to 1 : r^2= 0.999, indicative of a good quality fit. From the slope, we obtain : $H = 2.3$ eV, which is smaller than expected. One should recall that the present field configuration is different from the one of ref. 23 where the blade is mounted perpendicularly on a plane. The "sharply varying limit" of our field configuration can be obtained easily (eq. 50.5 in ref. 43) within the semi-classical approximation by integral of the wavevector in the tunneling region along x :

$$\frac{s}{F_a^2} = -2\int_0^{\lambda_t}\left(\frac{2m}{\hbar^2}\right)^{\frac{1}{2}}\left(H - qV_{ea}\frac{\lambda}{\lambda_a}\right)^{\frac{1}{2}}dx \tag{14}$$

where λ_t corresponds to the turning point : $\lambda_t = \lambda_a\frac{H}{qV_{ea}}$. This provides :

$$s = -\frac{2^{\frac{5}{2}}}{15}\frac{m^{\frac{1}{2}}}{q^2\hbar x_a}H^{\frac{5}{2}}. \tag{15}$$

Applying this model for the slope of fig. 6, we obtain : $H = 4.9$ eV, which is only slightly higher than the work function value $W = 4.5$ eV. As a result, the correction to be applied to the barrier height due to the blade geometry is small.

In summary, the 2 best functional forms with which to perform FN fits to our numerical results are : (1) the fit of $ln(j(F_a))$ as a function of $1/F_a$, with the usual work function in eq. 13. A reasonable enhancement factor is then obtained. (2) the "sharply varying limit" of ref. 23 but adapted to our field configuration, then the resulting barrier height H in eq. 15 is only slightly larger than the work function W. The differences between the present results on graphene edge and the ones of ref. 21 on graphene flat surface (in this case, the best linear fit is obtained for $ln(j(F_a)/F_a^{\frac{3}{2}})$ as a function of $1/F_a$) result from the change in the emitter geometry which impacts strongly the physical processes at play and the resulting emission levels.

C. Total energy distributions

Fig. 7 shows total energy distributions for different values of anode field up to the Fermi level energy. There is no emission above this energy because we assume 0 K materials. The distributions have a prominent step-like character which, similarly to fig. 4, is due to the discrete nature of the ϵ_{n_x} spectrum : emission increases sharply each time total energy becomes larger than one of the discrete energies ϵ_{n_x} because the corresponding level can start contributing to emission. These distributions can be fitted to exponentials $\propto e^{\frac{\epsilon}{\Delta\epsilon(F_a)}}$ and the corresponding energy widths are : $\Delta\epsilon(F_a) = 0.14$, 0.51 and 1.36 eV for anode fields $F_a =$ 0.25, 0.5 and 1 V/nm, respectively. TED width increases with applied fields, as expected since the tunneling barrier becomes a less efficient high energy filter as it becomes thinner.

We can discuss available measured[4,10,11] and computed[24–26] TED in the light of these results. TED width measurements are given as a function of the extraction voltage V_{ext} (fig. 10 in ref. 10), the latter can be translated into local cathode field $F_c = \beta_V V_{ext}$ using the voltage-to-field factor[10] : $\beta_V = 6.2\ 10^6\ \mathrm{m}^{-1}$. These results can be compared with ours if local cathode fields are identical in both conditions. This identity is achieved when :

$$F_c = F_a\beta_W = V_{ext}\beta_V. \tag{16}$$

Thus the cathode field for F_a=0.25 V/nm in our calculation would be identical to the one for V_{ext}=524 V in the experiment. The experimental TED width for this extraction voltage is $\Delta\epsilon$=0.29 eV, as seen from the linear relation shown on fig. 10 of ref. 10 :

$$\Delta\epsilon \approx 9.3\,10^{-4}\ V_{ext} - 0.195 \tag{17}$$

where $\Delta\epsilon$ is in eV, V_{ext} in Volt. This is of the same order of magnitude as a our result, 0.14 eV. We can similarly calculate the equivalent extraction voltages associated to $F_a = 0.5$ and 1 V/nm using eq. 16 and then obtain from eq. 17 the corresponding "experimental" widths 0.78 eV and 1.75 eV. This is in reasonable agreement with our results, 0.51 and 1.36 eV respectively. Larger "experimental" widths can be accounted for by larger temperature than in our model (0 K). In ref. 11, peak widths typically one order of magnitude larger $\Delta\epsilon \approx 2$ eV are shown. These larger widths may result, either from larger local fields, or from remaining impurities which can possibly broaden distributions[10].

Our results can also be compared with other TED width computations. The one of ref. 24,25 provides a distribution with typically $\Delta\epsilon \approx 1$ eV for a large cathode field $F_c = 10$ V/nm. This value is too large for our model to provide results to compare with. But using again the translation given by eq. 16 and the linear relation given by eq. 17, we obtain $\Delta\epsilon =$ 1.3 eV, consistent with the result of ref. 24,25. Notice finally that the width value given by the calculation of ref. 26, $\Delta\epsilon \approx 0.06$ eV for $F_c = 2$ V/nm, is only slightly smaller than the value given again by the combination of eq. 16 and eq. 17, which is $\Delta\epsilon = 0.1$ eV. It seems therefore possible to reconcile apparently contradictory results concerning TED widths by taking into account the dependence on field intensity observed in our model. It should be noticed however that to achieve this result, we had to use the linear relation (eq. 17) in a voltage range larger than the one on which it was observed experimentally[10].

IV. CONCLUSION

We presented in this paper a simple quantum perturbative full dimensionality model to study field emission from a graphene blade. The material electronic wavefunction is described by a translational invariant 2-dimensional square well potential designed to provide the correct Fermi level and a good approximation of the π graphene orbitals. The vacuum wavefunction is obtained by basis expansion for a separable electrostatic potential associated to an anode with a parabolic cylinder shape. Our model allows to discuss the usefulness of the different functional forms proposed to fit the emitted current intensity dependence on field. It also provides understanding of the lip patterns observed in emission experiments, as well as of the TED widths measurements. In future work, the present method could be adapted to better descriptions of the electronic structure of graphene, as provided for

instance by tight-binding[21] or density functional methods. It could also be extended to other materials of variable thicknesses, as our model compacts the description of the band structure of the emitting material in a limited number of adjustable parameters.

V. DATA STATEMENT

The data that support the findings of this study are available from the corresponding author upon reasonable request.

Appendix A: Material wavefunction

We enforce separability of the material electrostatic potential : $V_i(x,y,z) = V_{ix}(x)+V_{iy}(y)$ using a 1 dimension potential $V_{i\xi}$ ($\xi = x$ or y) given by :

$$\begin{aligned} &\text{If } |x-x_c| < \frac{L_x}{2} \ : \ V_{ix}(x) = 0 \ \text{ , else : } \ V_{ix}(x) = -V_0 \\ &\text{If } |y-y_c| < \frac{L_y}{2} \ : \ V_{iy}(y) = V_0 \ \text{ , else : } \ V_{iy}(y) = 0 \end{aligned} \tag{A1}$$

where $x_c = -\frac{L_x}{2}$ and $y_c = 0$.

The material electronic wavefunction associated to this separable potential reads : $\phi_{n_x n_y}(x,y) = \varphi_{n_x}(x)\varphi_{n_y}(y)$. The integers n_x and n_y are the quantum numbers associated to the discrete states bound in the one dimensional potentials along x and y. These states are given by the generic function $\varphi_{n_\xi}(\xi)$ ($\xi = x$ or y):

$$\begin{aligned} &\text{If } |\xi-\xi_c| < \frac{L_\xi}{2} \ : \ \varphi_{n_\xi}(\xi) = N_{\xi<} cos\left(k_{n_\xi}(\xi-\xi_c) + \frac{n_\xi \pi}{2}\right) \\ &\text{If } \xi-\xi_c \geq \frac{L_\xi}{2} \ : \ \varphi_{n_\xi}(\xi) = N_{\xi>} e^{-\kappa_{n_\xi}|\xi-\xi_c|} \\ &\text{If } \xi-\xi_c \leq -\frac{L_\xi}{2} \ : \ \varphi_{n_\xi}(\xi) = (-1)^{n_\xi} N_{\xi>} e^{-\kappa_{n_\xi}|\xi-\xi_c|} \end{aligned} \tag{A2}$$

which are symmetric or antisymmetric with respect to ξ_c according to the parity of n_ξ. Conservation of energy provides : $\frac{\hbar^2}{2m}k_{n_\xi}^2 - qV_0 = -\frac{\hbar^2}{2m}\kappa_{n_\xi}^2$ so that the 2 dimensional energy is : $\epsilon_{n_x\, n_y} = \frac{\hbar^2}{2m}\left(k_{n_x}^2 + k_{n_y}^2\right) - qV_0 = -\frac{\hbar^2}{2m}\left(\kappa_{n_x}^2 + \kappa_{n_y}^2\right) + qV_0$. Continuity at the interface $\xi = \xi_c + \frac{L_\xi}{2}$ gives the equation : $\tan\left(k_{n_\xi}\frac{L_\xi}{2} + \frac{n_\xi\pi}{2}\right) = \frac{\kappa_{n_\xi}}{k_{n_\xi}}$ the solution of which provides k_{n_ξ}. In particular, in the limit $V_0 \to +\infty$ we have : $k_{n_\xi} = \frac{(n_\xi+1)\pi}{L_\xi}$. Finally, normalization provides : $N_{\xi<}^2 = \frac{1}{\frac{L_\xi}{2}+\frac{1}{\kappa_{n_\xi}}}$.

Appendix B: Vacuum wavefunction

We describe in this appendix a method to obtain 2 dimensional electron wavefunctions $\psi_{\epsilon_{n_x}}(\lambda,\mu;V_{ea})$ in the inter-electrode region, following the methods described in ref. 38. The wavefunctions are solutions of an eigenvalue equation associated to the Hamiltonian of eq. 6 :

$$\left(-\frac{\hbar^2}{2m(\lambda^2+\mu^2)}\left(\frac{\partial^2}{\partial\lambda^2}+\frac{\partial^2}{\partial\mu^2}\right) - qV_e(\lambda)\right)\psi_{\epsilon_{n_x}}(\lambda,\mu;V_{ea}) = \epsilon_{n_x}\psi_{\epsilon_{n_x}}(\lambda,\mu;V_{ea}) \tag{B1}$$

These solutions are obtained in a domain bounded by the electrodes ($0 < \lambda < \lambda_a$) and an arbitrary line $\mu = \mu_M$ in vacuum which corresponds to the anode width and where the wavefunction is assumed to be 0. μ_M is chosen large enough so that the final result becomes insensitive to this parameter.

We first try to compute $\psi_{\epsilon_{n_x}}(\lambda, \mu; V_{ea})$ by expansion on a sine-type basis : $s_n^0(\mu) = \left(\frac{2}{\mu_M}\right)^{\frac{1}{2}} sin(k_n \mu)$ with : $k_n = \frac{(n+1)\pi}{\mu_M}$. These functions are normalized to 1 in the interval [0,μ_M] and are 0 at its ends. The expansion reads:

$$\psi_{\epsilon_{n_x}}(\lambda, \mu; V_{ea}) = \sum_n \Lambda^0_{n,\epsilon_{n_x}}(\lambda) s_n^0(\mu) \tag{B2}$$

where, here and below, the dependence on V_{ea} is dropped in the expansion for simplicity. Inserting this expansion in eq. B1, the coefficients $\Lambda^0_{n,\epsilon_{n_x}}(\lambda)$ are found to be solutions of a set of ordinary differential equations:

$$\frac{d^2 \Lambda^0_{n,\epsilon_{n_x}}(\lambda)}{d\lambda^2} = \sum_{n'} R^{\epsilon_{n_x}}_{nn'}(\lambda) \Lambda^0_{n',\epsilon_{n_x}}(\lambda) \tag{B3}$$

where the elements of the coupling matrix $\mathbf{R}^{\epsilon_{n_x}}(\lambda)$ are given by :

$$R^{\epsilon_{n_x}}_{nn'}(\lambda) = k_n^2 \delta_{nn'} - \frac{2m}{\hbar^2} \left(q V_e(\lambda) + \epsilon_{n_x}\right) \left(\lambda^2 \delta_{nn'} + < s_n^0 | \mu^2 | s_{n'}^0 >\right) \tag{B4}$$

with :

$$\begin{aligned} < s_n^0 | \mu^2 | s_{n'}^0 > &= \int_0^{\mu_M} d\mu s_n^0(\mu) \mu^2 s_{n'}^0(\mu) = \mu_M^2 \left(\frac{1}{3} - \frac{1}{2(n+1)^2 \pi^2}\right) \quad \text{if } n = n' \\ &= \mu_M^2 \frac{8(-1)^{n+n'}(n+1)(n'+1)}{\pi^2 (n+n'+2)^2 (n-n')^2} \quad \text{otherwise} \end{aligned}$$

$\delta_{nn'}$ is a Kronecker symbol. As these couplings persist even at large λ, we expand instead the wavefunction on a set of N eigenvectors $s_n^{\epsilon_{n_x}}(\mu; \lambda)$ (associated to eigenvalues $r_n^{\epsilon_{n_x}}(\lambda)$) of the $\mathbf{R}^{\epsilon_{n_x}}(\lambda)$ matrix :

$$\psi_{n_0\, \epsilon_{n_x}}(\lambda, \mu; V_{ea}) = \sum_{n=1}^{N} \Lambda_{n, n_0\, \epsilon_{n_x}}(\lambda) s_n^{\epsilon_{n_x}}(\mu; \lambda) \tag{B5}$$

The couplings between the $s_n^{\epsilon_{n_x}}(\mu; \lambda)$ now vanish at large λ. For each ϵ_{n_x} value, there is a set of $n_0 = 1 - N$ linearly independent regular solutions $\Lambda_{n, n_0\, \epsilon_{n_x}}(\lambda)$. As we need to compute them all, we have added the n_0 subscript in eq. B5. These solutions are obtained with the diabatic-by-sector method by propagation from small to large λ. The

initial boundary conditions are : $\Lambda_{n,n_0\,\epsilon_{n_x}}(\lambda) \xrightarrow[\lambda\to 0]{} 0$ (regular solutions) and $\frac{d\Lambda_{n,n_0\,\epsilon_{n_x}}(\lambda)}{d\lambda} \xrightarrow[\lambda\to 0]{} \delta_{n\,n_0}$. At sufficiently large λ : $\lambda \geq \lambda_M$, $r_n^{\epsilon_{n_x}}(\lambda)$ can be approximated by a cubic form :

$$r_n^{\epsilon_{n_x}}(\lambda) \approx c_n(\epsilon_{n_x})\,(\lambda - \lambda_0^n(\epsilon_{n_x}))^3 \tag{B6}$$

Usually, $c_n(\epsilon_{n_x})$ is negative and $\lambda_0^{\epsilon_{n_x}}$ positive. Approximate asymptotic forms for $\Lambda_{n,n_0\,\epsilon_{n_x}}(\lambda)$ are thus obtained as linear combinations of the asymptotic forms:

$$\Lambda^{\pm}_{n,\epsilon_{n_x}}(\lambda) = (\lambda - \lambda_0^n(\epsilon_{n_x}))^{-\frac{3}{4}}\, e^{\pm i\frac{2}{5}(-c_n(\epsilon_{n_x}))^{\frac{1}{2}}\left(\lambda-\lambda_0^n(\epsilon_{n_x})\right)^{\frac{5}{2}}} \tag{B7}$$

Another set of N solutions regular for $\lambda = 0$ and associated to scattering matrix (S)-type asymptotic boundary conditions can be written as :

$$\psi^{(S)}_{n_0\,\epsilon_{n_x}}(\lambda,\mu;V_{ea}) = \sum_{n=1}^{N} \Lambda^{(S)}_{n,n_0\,\epsilon_{n_x}}(\lambda) s_n^{\epsilon_{n_x}}(\mu;\lambda) \tag{B8}$$

with :

$$\Lambda^{(S)}_{n,n_0\,\epsilon_{n_x}}(\lambda) \xrightarrow[\lambda\to+\infty]{} N_{n,n_0\,\epsilon_{n_x}}\left(\Lambda^{+}_{n,\epsilon_{n_x}}(\lambda)\delta_{nn_0} - \Lambda^{-}_{n,\epsilon_{n_x}}(\lambda)\mathrm{S}^{*}_{nn_0}(\epsilon_{n_x})\right) \tag{B9}$$

As the regular solutions of the two sets $\Lambda_{n,n_0\,\epsilon_{n_x}}(\lambda)$ and $\Lambda^{(S)}_{n,n_0\,\epsilon_{n_x}}(\lambda)$ $(n_0 = 1-N)$ span the same space, they are linear combinations of each others, which reads in matrix form: $\mathbf{\Lambda}^{(S)}_{\epsilon_{n_x}}(\lambda) = \mathbf{\Lambda}_{\epsilon_{n_x}}(\lambda)\mathbf{A}_{\epsilon_{n_x}}$ and $\frac{d\mathbf{\Lambda}^{(S)}_{\epsilon_{n_x}}(\lambda)}{d\lambda} = \frac{d\mathbf{\Lambda}_{\epsilon_{n_x}}(\lambda)}{d\lambda}\mathbf{A}_{\epsilon_{n_x}}$ where $\mathbf{A}_{\epsilon_{n_x}}$ is the $N\times N$ matrix of the coefficients of these linear combinations. Solving these linear equations provides the $\mathbf{A}_{\epsilon_{n_x}}$ and (S) matrices.

The N solutions $\psi^{(S)}_{n_0\,\epsilon_{n_x}}(\lambda,\mu)$ are orthonormal and the condition :

$$\langle\psi^{(S)}_{n_0\,\epsilon_{n_x}}|\psi^{(S)}_{n_0'\,\epsilon_{n_x'}}\rangle = \int\int d\lambda d\mu(\lambda^2+\mu^2)\psi^{(S)\,*}_{n_0\,\epsilon_{n_x}}(\lambda,\mu;V_{ea})\psi^{(S)}_{n_0'\,\epsilon_{n_x'}}(\lambda,\mu;V_{ea}) = \delta(\epsilon_{n_x}-\epsilon_{n_x'})\,\delta_{n_0\,n_0'} \tag{B10}$$

where the first δ is the Dirac function and the second one the Kronecker symbol, provides, using the normalization method described in appendix A of ref. 44 :

$$N^2_{n,n_0\,\epsilon_{n_x}} = \frac{m}{2\pi\hbar^2(-c_n(\epsilon_{n_x}))^{\frac{1}{2}}} \tag{B11}$$

* Electronic address: bruno.lepetit@irsamc.ups-tlse.fr

[1] L. Chen, H. Yua, J. Zhong, L. Song, J. Wuc, and W. Su, Materials Science and Engineering B, **220**, 44 (2017).

[2] Y. S. Ang, S.-J. Liang, and L. K. Ang, MRS Bulletin **42**, 505 (2017).

[3] F. Giubileo, A. D. Bartolomeo, L. Iemmo, and G. Luongo, Appl. Sci. **8**, 526 (2018).

[4] S. T. Purcell, P. Vincent, S. Perisanu, A. Ayari, and P. Poncharal, in *Nanostructured Carbon Electron Emitters and Their Applications*, edited by Y. Saito (Jenny Stanford, 2022), pp. 127–148.

[5] Z. Xiao, J. She, S. Deng, Z. Tang, Z. Li, J. Lu, and N. Xu, ACS Nano **4**, 6332 (2010).

[6] S. Santandrea, F. Giubileo, V. Grossi, S. Santucci, M. Passacantando, T. Schroeder, G. Lupina, and A. D. Bartolomeo, App. Phys. Lett. **98**, 163109 (2011).

[7] J. Xu, Q. Wang, Z. Tao, Z. Qi, Y. Zhai, S. Wu, X. Zhang, and W. Lei, ACS Appl. Mater. Interfaces **8**, 3295 (2016).

[8] K. Nakakubo, K. Asaka, H. Nakahara, and Y. Saito, App. Phys. Express **5**, 055101 (2012).

[9] N. Yokoyama, K. Nakakubo, K. Iwata, K. Asaka, H. Nakahara, and Y. Saito, Surf. Interface Anal. **48**, 1217 (2016).

[10] R. Diehl, M. Choueib, S. Choubak, R. Martel, S. Perisanu, A. Ayari, P. Vincent, S. T. Purcell, and P. Poncharal, Phys. Rev. B **102**, 035416 (2020).

[11] J. L. Shaw, J. B. Boos, B. D. Kong, J. T. Robinson, and G. G. Jernigan, J. Appl. Phys. **125**, 054502 (2019).

[12] R. H. Fowler and L. Nordheim, Proceedings of the Royal Society of London A: Mathematical, Physical and Engineering Sciences **119**, 173 (1928).

[13] L. W. Nordheim, Proc. R. Soc. London, Ser. A **121**, 626 (1928).

[14] R. Burgess, H. Kroemer, and J. Houston, Phys. Rev. **90**, 515 (1953).

[15] E. L. Murphy and R. H. Good, Physical Review **102**, 1464 (1956).

[16] J. He, P. H. Cutler, and N. M. Miskovsky, App. Phys. Lett. **59**, 1644 (1991).

[17] R. G. Forbes, App. Phys. Lett. , **89**, 113122 (2006).

[18] A. Modinos, Solid-State Electronics **45**, 809 (2001).

[19] R. G. Forbes, J. H. B. Deane, A. Fischer, and M. S. Mousa, Jordan Journal of Physics **8**, 125

(2015).

[20] Y. Ang and L. Ang, 31st International Vacuum Nanoelectronics Conference (IVNC), Kyoto, p. 1 (2018).

[21] B. Lepetit, J. Appl. Phys. **129**, 144302 (2021).

[22] P. Zhang, Y. S. Ang, A. L. Garner, Á. Valfells, J. L. Luginsland, and L. K. Ang, J. Appl. Phys. **129**, 100902 (2021).

[23] X.-Z. Qin, W.-L. Wang, N.-S. Xu, Z.-B. Li, and R. G. Forbes, Proc. R. Soc. A **467**, 1029 (2011).

[24] K. Tada and K. Watanabe, Phys. Rev. Lett. **88**, 127601 (2002).

[25] M. Araidai, Y. Nakamura, and K. Watanabe, Phys. Rev. B **70**, 245410 (2004).

[26] S. F. Huang, T. C. Leung, B. Li, and C. T. Chan, Phys. Rev. B **72**, 035449 (2005).

[27] M. Márquez-Mijares, B. Lepetit, and D. Lemoine, Surface Science **645**, 56 (2016).

[28] M. Márquez-Mijares, B. Lepetit, D. Lemoine, K. Almaksour, M. J. Kirkpatrick, P. Dessante, E. Odic, D. Alamarguy, F. Bayle, P. Teste, et al., J. Vac. Sci. Technol. B **34**, 061208 (2016).

[29] Y. Gao and S. Okada, Carbon **142**, 190 (2019).

[30] Z. Li, N. Xu, and H. J. Kreuzer, Phys. Rev. B **85**, 115427 (2012).

[31] M. Luo and Z. Li, J. App. Phys. **120**, 204304 (2016).

[32] B. Lepetit, D. Lemoine, and M. Márquez-Mijares, J. App. Phys. **120**, 085105 (2016).

[33] B. Lepetit, J. Appl. Phys. **122**, 215105 (2017).

[34] B. Lepetit, J. App. Phys. **125**, 025107 (2019).

[35] R. Clementi and C. Roettl, Atomic data and nuclear data tables **14**, 186 (1974).

[36] S. de Vega and F. J. Garcia de Abajo, ACS Photonics **4**, 23672375 (2017).

[37] A. H. Castro-Neto, F. Guinea, N. M. R. Peres, K. S. Novoselov, and A. K. Geim, Rev. Mod. Phys. **81**, 109 (2009).

[38] B. Lepetit, J. M. Launay, and M. Le Dourneuf, Chem. Phys. **106**, 103 (1986).

[39] J. Bardeen, Phys. Rev. Lett., **6**, 57 (1961).

[40] H. Yamaguchi, K. Murakami, G. Eda, T. Fujita, P. Guan, W. Wang, C. Gong, J. Boisse, S. Miller, M. Acik, et al., acs nano **5**, 4945 (2011).

[41] W. H. Press, S. A. Teukolsky, W. T. Vetterling, and B. P. Flannery, *Numerical recipies. The art of scientific computing.* (Cambridge University Press, 2007), 3rd ed.

[42] S. Watcharotone, R. S. Ruoff, and F. H. Read, Physics Procedia **1**, 71 (2008).

[43] L. D. Landau and E. M. Lifshitz, *Quantum mechanics. Non relativistic theory. Course of theo-*

retical physics. Vol. 3 (Butterworth Heinemann, 1977), 3rd ed.

[44] M. S. Child, *Molecular collision theory* (Academic Press, 1974).

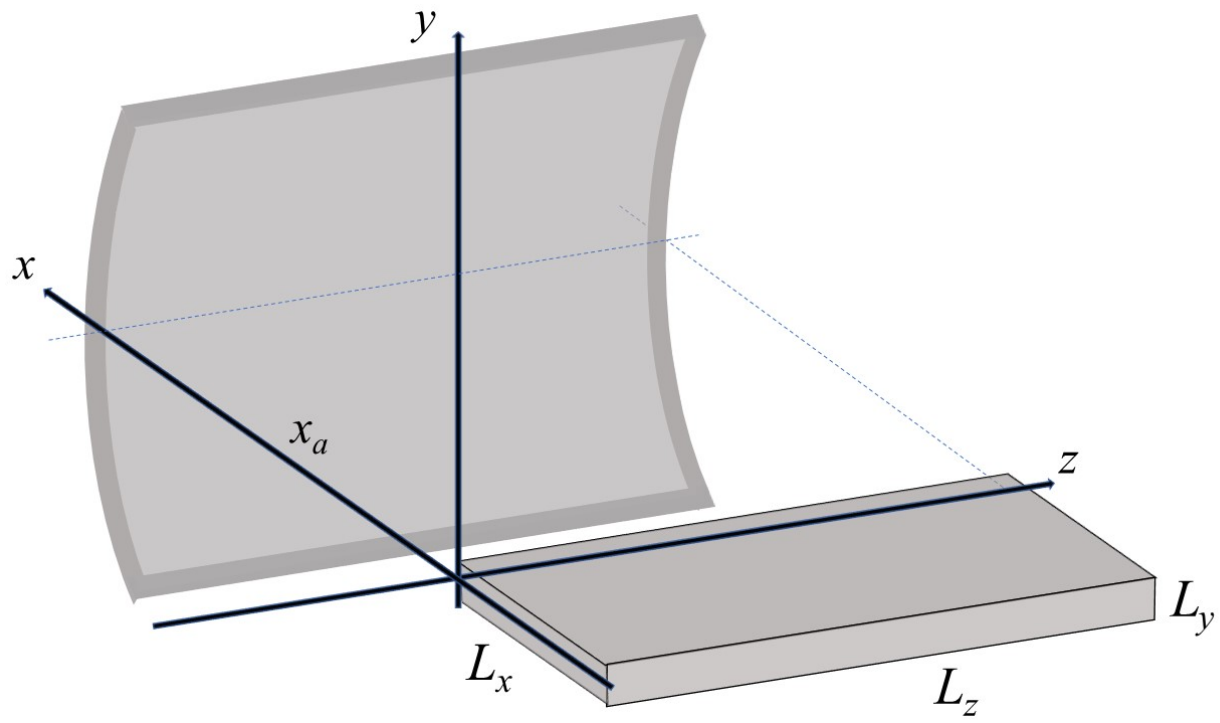

FIG. 1: The electrode configuration. A graphene blade cathode L_y thick and of area $L_x\, L_z$ located in the $(x \leq 0, z)$ half-plane is facing a parabolic cylinder anode parallel to the z axis.

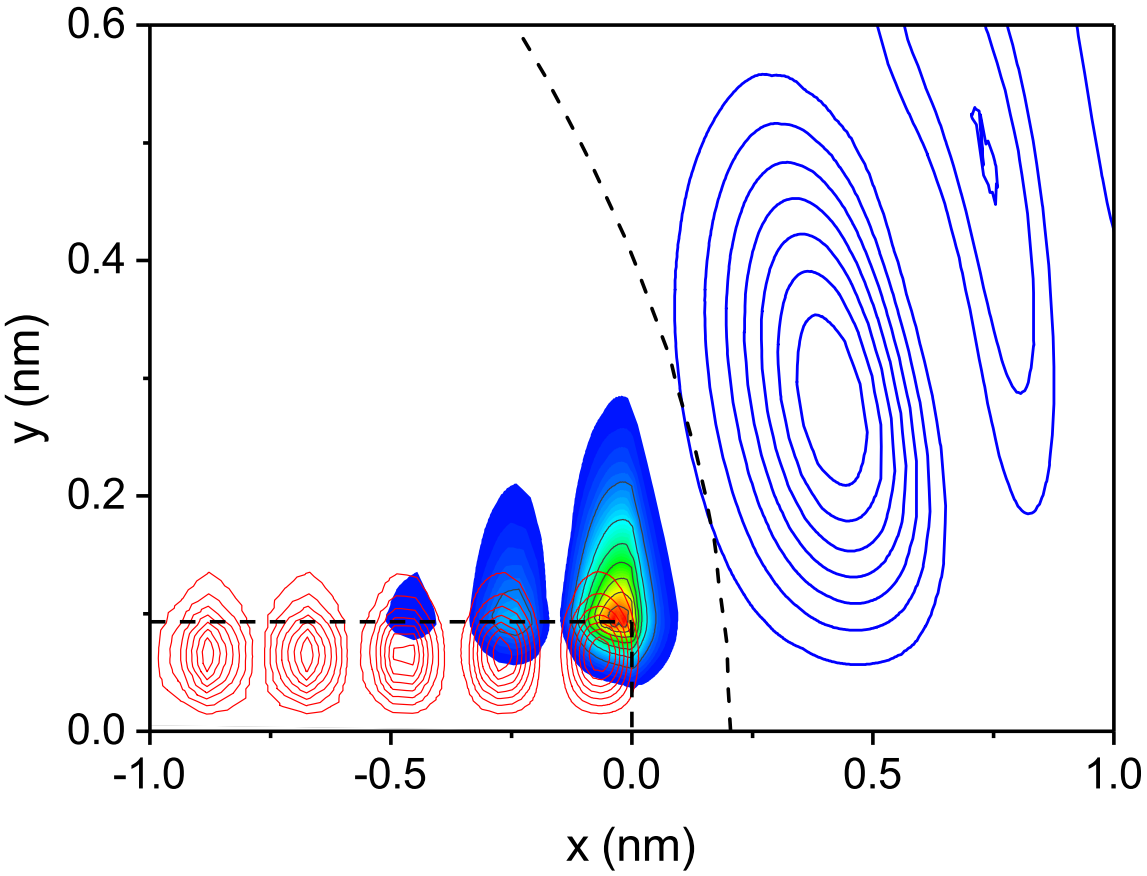

FIG. 2: Bottom left dashed rectangle : boundaries of the graphene blade domain $x \leq 0$, $y \leq L_y/2$ = 0.093 nm, it corresponds to the discontinuities of the graphene potential (eq. A1). Red contours : the graphene bound state $|\phi_{n_x}(x,y)|^2$ (eq. 1) with $n_y = 1$ to mimic a π_y orbital and $n_x = 98$ to have a state as close as possible in energy to the Fermi level for $L_x = 20$ nm. Blue contour : the inter-electrode wavefunction squared $|\psi^{(S)}_{n_0\,\epsilon_{n_x}}(\lambda,\mu;V_{ea})|^2$ (eq. B8) for the same n_x and for n_0 chosen so that $\psi^{(S)}_{n_0\,\epsilon_{n_x}}$ has maximum overlap with ϕ_{n_x}. $F_a = 0.5$ V/nm (i.e. $x_a = 100$ nm, $V_{ea} =$ 100 V). Color filled contours : the square of the norm of the Bardeen overlap $|m_{n_0 n_x}(\lambda,\mu;V_{ea})|^2$ (eq. 11) for this pair of states. Curved black dashed line : limit of the tunneling region at the Fermi level energy : $qV_e(\lambda) = W$. The contour plots are in arbitrary units.

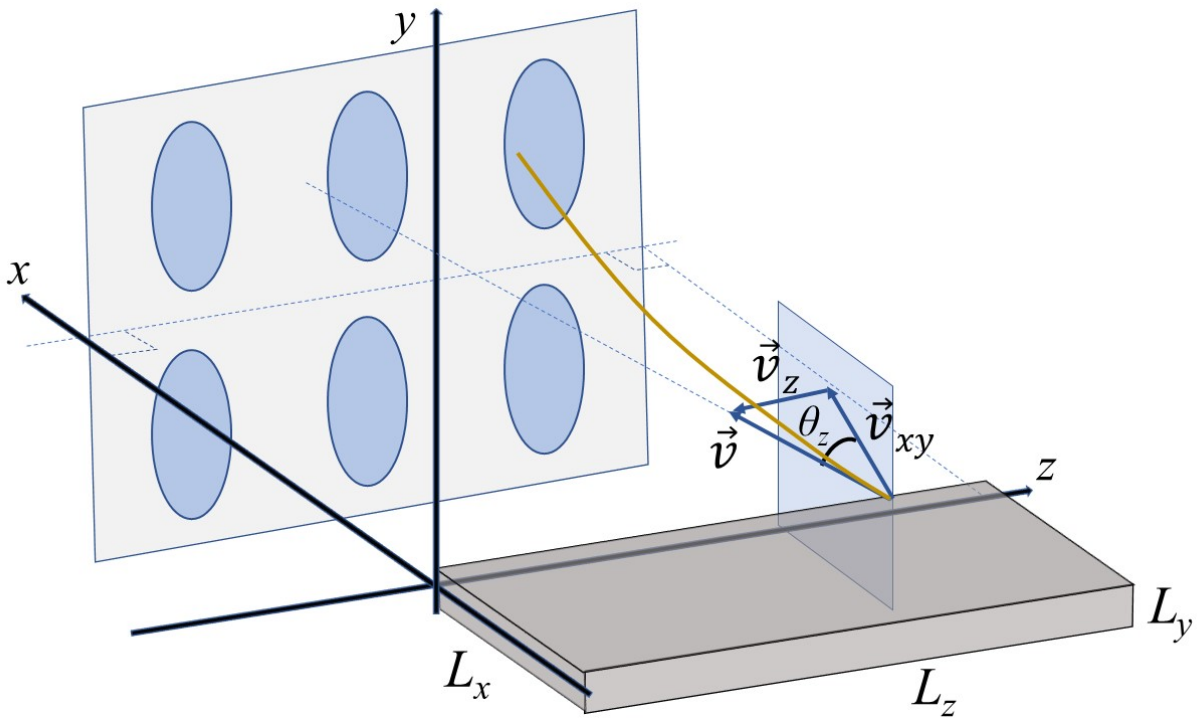

FIG. 3: Schematics of a three-fold "lip pattern" observed on a screen in the $(y\,z)$ plane facing the half $(x\,z)$ plane cathode. The trajectory of an electron emitted with the initial speed $\vec{v} = \vec{v}_{xy} + \vec{v}_z$ (components in and out the $(x\,y)$ plane) is depicted. The angle θ_z measures the deviation from the $(x\,y)$ plane of the emitted electron trajectory : $\tan(\theta_z) = \frac{v_z}{v_{xy}}$.

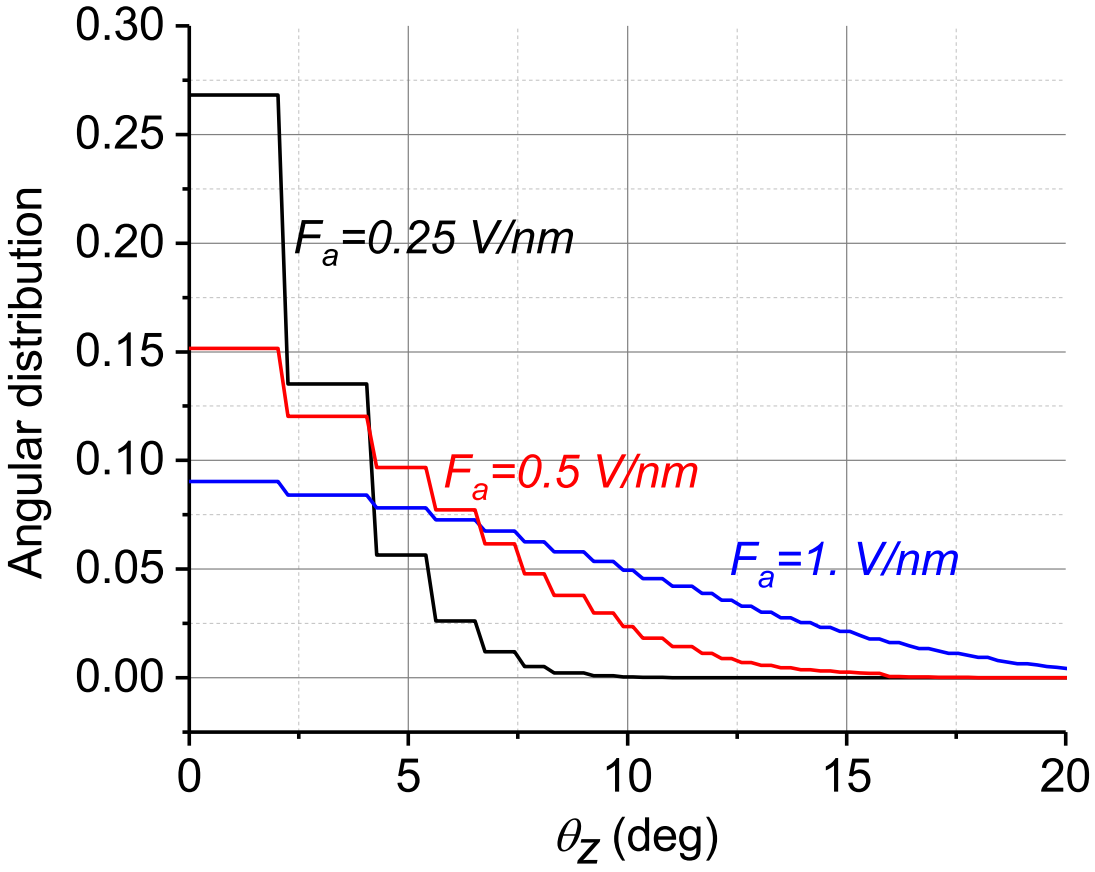

FIG. 4: Normalized (its integral over angle equals 1) angular distribution of the emitted electrons. The angle θ_z is the one between the z-axis and the xy-plane components of the emitted electron speed. Three different anode fields $F_a = 0.25$, 0.5 and 1 V/nm are considered. The blade width is $L_x = 30$ nm.

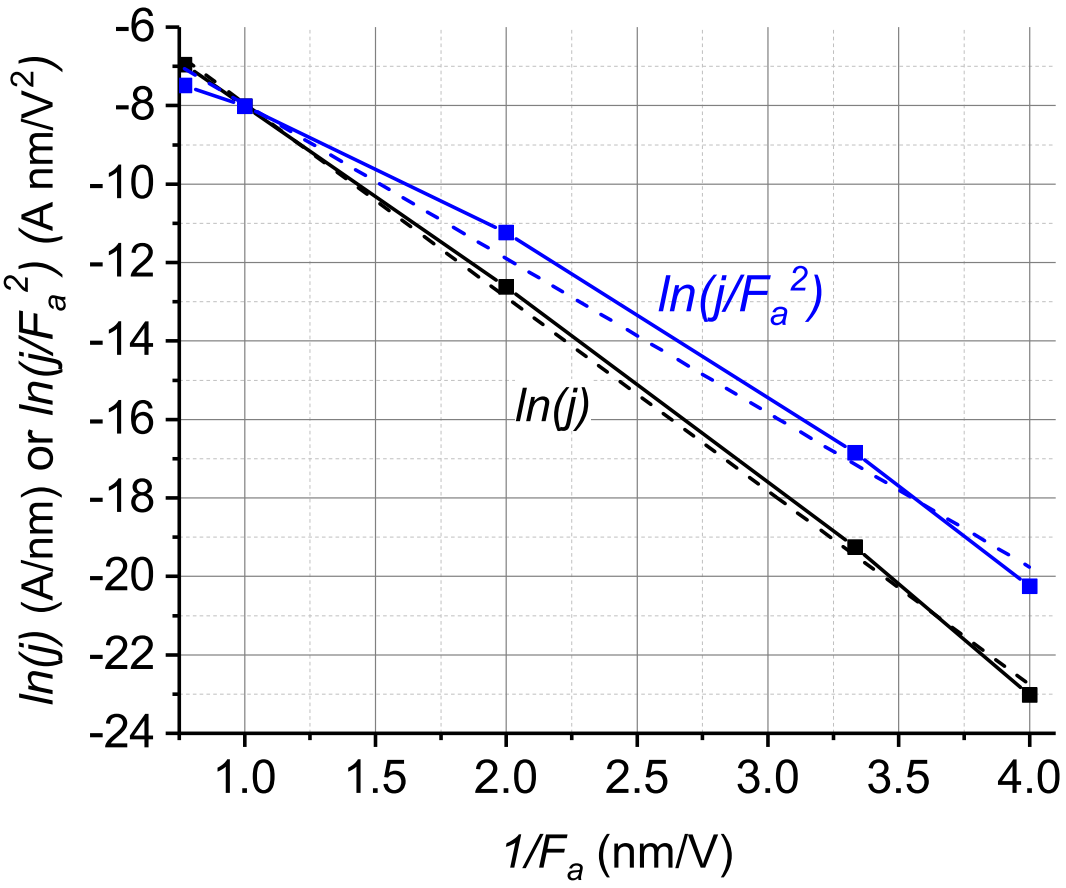

FIG. 5: FN-type plot of the emitted current, as a function of the inverse of the anode field $1/F_a$ at $x_a = 100$ nm. Both functions, $ln(j)$ (black) and $ln(j/F_a^2)$ (blue) are shown. The linear fits of these functions are shown as dashed lines. The coefficients of determination of these fits are r^2= 0.992 for $ln(j/F_a^2)$ and r^2= 0.999 for $ln(j)$. The blade width is $L_x = 30$ nm.

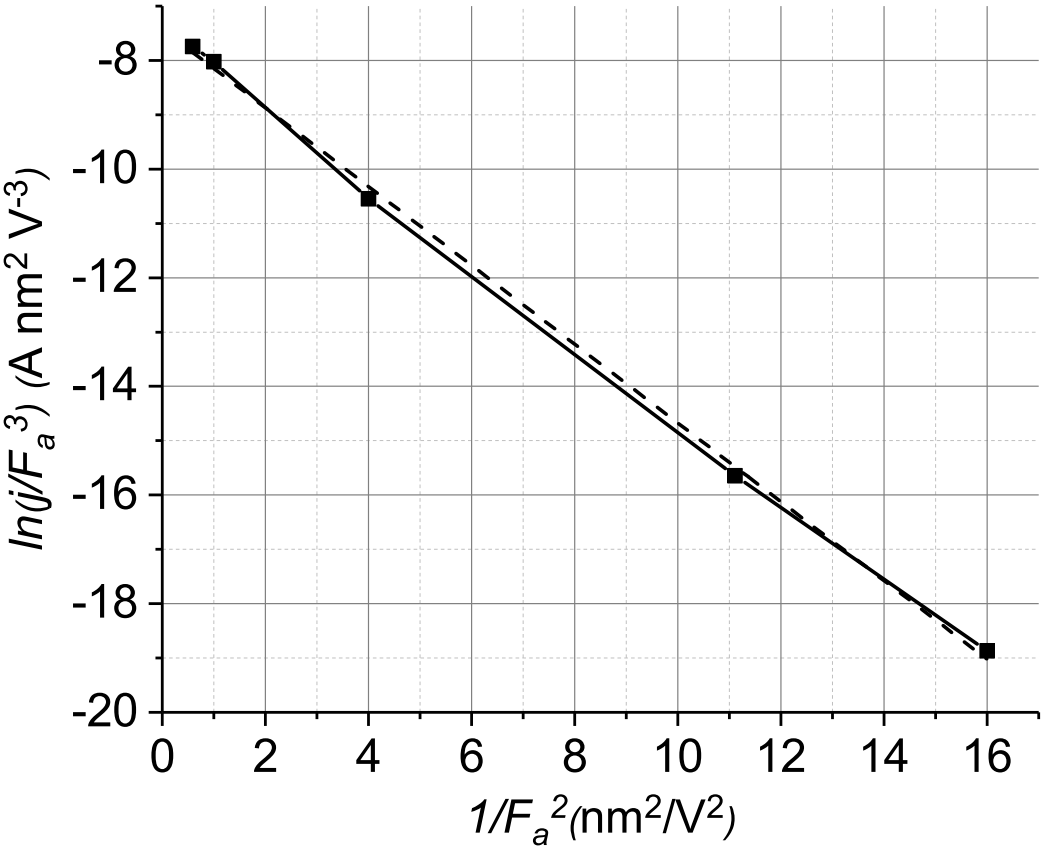

FIG. 6: FN-type plot of the emitted current : $ln(j/F_a^3)$ is shown as a function of $1/F_a^2$ (full line + symbols), the anode being located at $x_a = 100$ nm. This follows the prescription of eq. 6.15, ref. 23 in the "sharply varying field" limit. Dashed line : the linear fit of these data. The coefficient of determination of the fit is r^2= 0.998. The blade width is $L_x = 30$ nm.

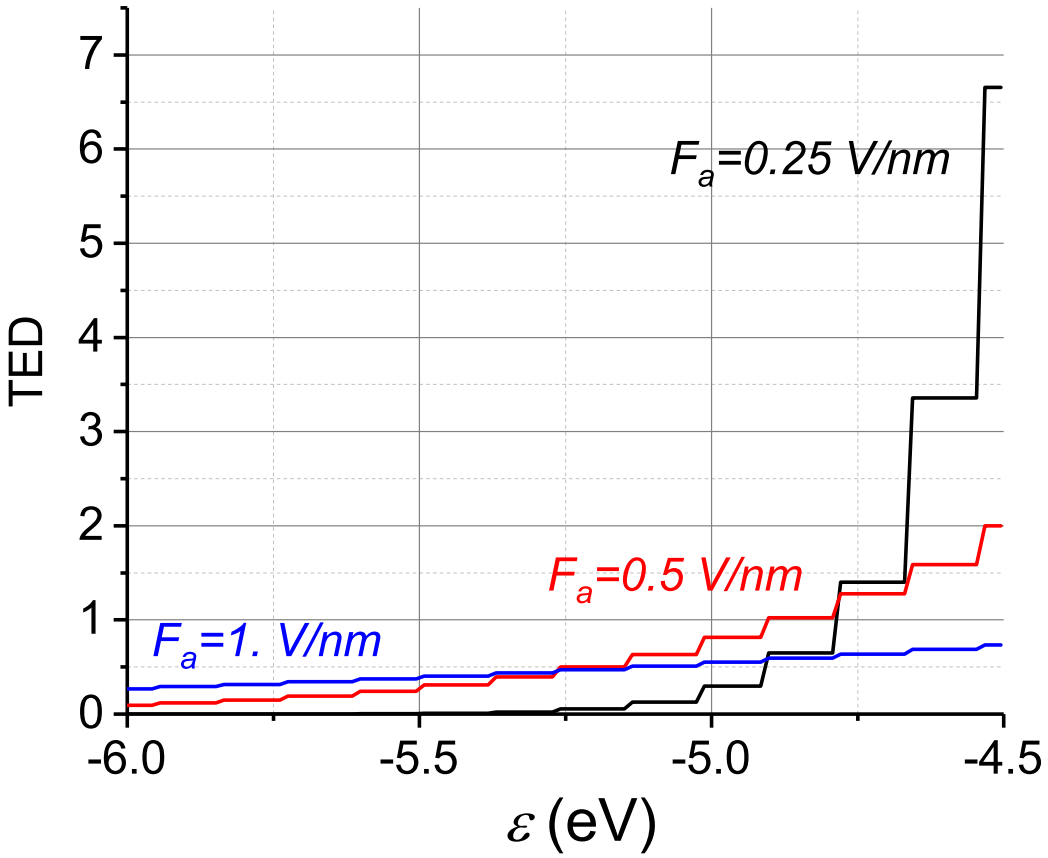

FIG. 7: Normalized (its integral over energy equals 1) total electrons energy distribution (TED) for 3 different anode fields $F_a = 0.25$, 0.5 and 1 V/nm. The blade width is $L_x = 30$ nm.